

Energy Landscapes of Carbon Clusters from Tight-Binding Quantum Potentials

David Furman,^{*,†} Fedor Naumkin,^{*,‡} and David J. Wales^{*,†}

*Department of Chemistry, University of Cambridge, Lensfield Road, Cambridge CB2 1EW,
United Kingdom, and Faculty of Science, Ontario Tech University/UOIT, Oshawa,
Ontario L1G 0C5, Canada*

E-mail: df398@cantab.ac.uk; Fedor.Naumkin@uoit.ca; dw34@cam.ac.uk

Abstract

We calculate transformation pathways between fullerene and octahedral carbon clusters and between a buckyball and its bowl-shaped isomer. The energies and gradients are provided by efficient tight-binding potentials, which are interfaced to our Energy Landscape exploration software. From the global energy landscape, we extract the mechanistic and kinetic parameters as a function of temperature, and compare our results to selected density functional theory (DFT) (PBE/cc-pVTZ) benchmarks. Infrared spectra are calculated to provide data for experimental identification of the clusters and differentiation of their isomers. Our results suggest that the formation of buckyballs from a buckybowl will be suppressed at elevated temperatures (above around 5250 K) due to entropic effects, which may provide useful insight into the detection of cosmic fullerenes.

^{*}To whom correspondence should be addressed

[†]Department of Chemistry, University of Cambridge, Lensfield Road, Cambridge CB2 1EW, United Kingdom

[‡]Faculty of Science, Ontario Tech University/UOIT, Oshawa, Ontario L1G 0C5, Canada

Introduction

Carbon is perhaps the most versatile chemical element on Earth. On the nanoscale, carbon exhibits a rich and complex phase diagram, featuring fullerenes, nanotubes, nano-onions and diamondoids.¹ Recently, a new class of octahedral carbon clusters with significant stability has been reported, featuring tetragonal rings. Unexpectedly, the rings offer an energy efficient means of transforming graphene sheets into three-dimensional spheroid shapes, similar to fullerenes.² Fullerenes are also a relatively recent addition to the inventory of known cosmic species. A key question to be resolved in the context of circumstellar and interstellar fullerenes is where and how they are formed,^{3,4} and whether they contribute to the infrared emission spectra of planetary and proto-planetary nebulae, including the broad plateau between 6-9 μm .⁵

Over the past two decades, many different models have been proposed to explain the formation of fullerenes from graphite, including the ‘pentagon road’,^{6,7} the ‘fullerene road’,⁸ ‘ring coalescence’⁹ and the ‘shrinking hot giant model’.¹⁰ Although there is a large body of experimental evidence supporting such bottom-up mechanisms,¹¹⁻¹³ they are almost entirely based on mass spectrometry, which analyses only gas phase species. Computational methods provide complementary insights on mechanisms, electronic states and material properties of fullerenes and their isomers.¹⁴⁻¹⁷ Recent in-situ tunneling electron microscopy experiments have demonstrated that a direct transformation of flat graphene sheets to fullerene cages is possible, and includes folding a bowl-shaped intermediate structure.¹⁸ The latest study joins earlier reports^{19,20} that focus on top-down formation routes. Buckybowls also serve as key intermediates in bottom-up synthesis routes, such as condensation from small dimers and clusters at elevated temperatures.²¹⁻²⁴ In contrast, the formation and transformation pathways of octahedral clusters have not been reported before.

In this study, we calculate complete transformation pathways between octahedral 24-atom and 32-atom carbon clusters and the respective fullerenes, as well as the pathway between a buckyball and a buckybowl, using the Computational Energy Landscape methodology.²⁵

We compare two quantum-based potentials (SCC-DFTB and GFN2-xTB) to obtain global energy landscapes for these systems, together with the associated transformation kinetics and mechanisms. To facilitate experimental detection efforts, we provide DFT level (PBE0/cc-pVDZ) infrared (IR) spectra and discuss their features.

Methods

Tight-Binding Quantum Potentials and DFT

For all the calculations reported in this study, we have compared two alternative tight-binding potentials. The first method (SCC-DFTB) is a well-established approximation for DFT, which is parameterised with a minimal basis set. The DFTB+ software package²⁶ (version 19.1) has been interfaced to our OPTIM²⁷ and PATHSAMPLE²⁸ codes, and provides the energies and gradients needed for all the geometry optimisation routines. Specifically, we have employed the self-consistent charge DFTB3 model²⁹ and the 3ob-3-1 parameter set,³⁰ which offer increased accuracy compared to previous models. The self-consistency tolerance was chosen as $10^{-10} e$. The second method is GFN2-xTB,³¹ which is a more recent tight-binding model with multipole electrostatics and density-dependent dispersion interactions (version 6.3.2). It employs global and element-specific parameters and is expected to have useful accuracy and transferability with a modest computational cost. An interface to OPTIM was again employed to provide the energies and gradients. The chosen energy accuracy in GFN2-xTB was better than $10^{-6} E_h$.

As a benchmark, we have additionally calculated connected pathways for C_{24} and C_{32} using DFT with the PBE functional, as implemented in Gaussian 09.³² The cc-pVTZ basis set was used for the C_{24} cluster, and the minimal STO-3G basis set was used for C_{32} . In a second step, single point energies were recalculated for the C_{32} pathway using the cc-pVTZ basis. The infrared (IR) spectra were calculated at the PBE0/cc-pVDZ level.

Exploring the Energy Landscapes

The first stage in our approach is to find a kinetically relevant pathway between the reactant and product using geometry optimisation tools implemented in the OPTIM²⁷ program. Discrete pathways are constructed as a sequence of transition states and the minima they connect via steepest-descent paths.²⁵ Double-ended searches were performed between pairs of local minima, starting from a doubly-nudged^{33,34} elastic band^{35,36} (DNEB) interpolation. The images corresponding to local maxima are taken as candidate transition states and refined accurately using hybrid eigenvector-following.³⁷⁻⁴⁰ The connectivity is then checked by calculating the two steepest-descent paths that lead downhill in energy from each transition state. For incomplete connections, further pairs of minima were chosen as end points for additional DNEB runs using the missing connection algorithm.⁴¹ Once an initial connected path is found, it is refined by a repeated application of procedures available in PATHSAMPLE to search for pathways with lower barriers and shorter path lengths.⁴¹⁻⁴³ The database refinement process is continued until the phenomenological rate constants⁴⁴ converge to within an order of magnitude. To remove artificial kinetic traps from the growing kinetic network we identify pairs of minima for connection based on the ratio of the potential energy barrier to the potential energy difference from the product.⁴² Hence, minima having low potential energy, but separated from the product region by high barriers, are likely to be selected. The final databases of minima and transition states correspond to converged kinetic transition networks, which can be visualised using disconnectivity graphs.^{45,46}

To extract rate constants for the pathways, one needs to account for the ensemble populations of endpoints at any given temperature. The measured experimental rate is the transition rate between these ensembles. Thus, we define product and reactant free energy groups according to a free energy difference threshold between the transition states and associated minima via a self-consistent regrouping scheme.⁴⁷ These groups represent the reactant and product ensembles in local equilibrium (macrostates), providing a direct comparison with experimental rates. To calculate the rate constants between any two con-

nected minima, we use transition state theory^{48,49} and harmonic vibrational densities of states. The phenomenological two-state rate constants between reactants and products can then be extracted from the database using the graph transformation approach.^{50,51} The rate constants obtained in this way involve a Markov assumption, and we also employ harmonic vibrational densities of states throughout. Although the Markov approximation is liable to break down for minima separated by low barriers, these steps are not rate determining, and so the largest uncertainties in the phenomenological rate constants probably arise from the underlying approximate potentials. The input files for all calculations are provided as supporting information.

Results and Discussion

Energy Landscapes

Octahedral to Fullerene

We begin our analysis with the disconnectivity graphs^{45,46} for C_{24} and C_{32} in Figs. 1 to 4, respectively. Starting with SCC-DFTB, Fig. 1 presents the various minima that lie within roughly $2 E_h$ of the global minimum, which is the C_{24} fullerene endpoint at the bottom of the graph. The overall landscape can be considered funnel-like,⁵²⁻⁵⁴ which suggests that transformation from any high-energy structures to the global minimum should be achieved relatively easily, provided that enough thermal energy is available. Among the low-lying structures, the octahedral C_{24} cluster is relatively stable and lies $0.024 E_h$ above the global minimum. The high-energy minima result from various cage breaks, which naturally make them relatively unstable, especially if dangling chains are present, such as the structure shown in the upper-left part of Fig. 1. Compared to SCC-DFTB, Fig. 2 shows that GFN2-xTB also ranks the fullerene structure as the more stable species, albeit with a significantly reduced gap of $0.002 E_h$. Previous DFT calculations² have found the octahedral cluster to lie

within $0.03\text{-}0.04 E_h$ above the fullerene structure for a triplet spin state, which was reported to be more stable than the singlet state for this system. In our tests, repeated single-point energy calculations in the triplet state led to an increase in energy for both clusters and both potentials.

A more significant difference between the potentials, however, is that the fullerene is not the global minimum using GFN2-xTB. In fact, a careful inspection reveals that there are three additional structures of lower energy (see Fig. S1 in supporting information). One of them (#7 in Fig. S1) has an energy of $-50.758 E_h$ and is practically indistinguishable from the fullerene, lying $0.006 E_h$ below it. The rest are isomers with two square faces. In the first isomer (#26 in Fig. S1) with an energy of $-50.756 E_h$, one square face is attached to 2 pentagons and 2 hexagons, and the other square is attached to 1 pentagon and 3 hexagons. In the second isomer (#27 in Fig. S1) with an energy of $-50.759 E_h$, both square faces are attached to 2 pentagons and 2 hexagons. Lastly, in contrast to SCC-DFTB, the high-energy structures for the GFN2-xTB potential seem to lack any dangling chains at this energy range.

Results for C_{32} are presented in Figs. 3-4. The general structure remains funneled, which suggests that the system should transform easily from any open, high-energy state to the global minimum structure (fullerene). The octahedral structure lies $0.182 E_h$ and $0.216 E_h$ above the global minimum for SCC-DFTB and GFN2-xTB, respectively. These energy differences agree well with previous² DFT results, which reported a difference of $0.231 E_h$. Both potentials reveal the presence of some relatively stable outliers behind fairly high barriers (shown to the left of the octahedral cluster in Figs. 3-4). These structures correspond to the presence of heptagonal and octagonal faces. In the case of SCC-DFTB, an octagonal face is connected to 3 squares, 3 pentagons and 2 hexagons, while for GFN2-xTB the leftmost structure contains 3 heptagons and a triangle of carbons. The second unexpected structure contains an octagon, which is connected to 4 squares and 4 hexagons.

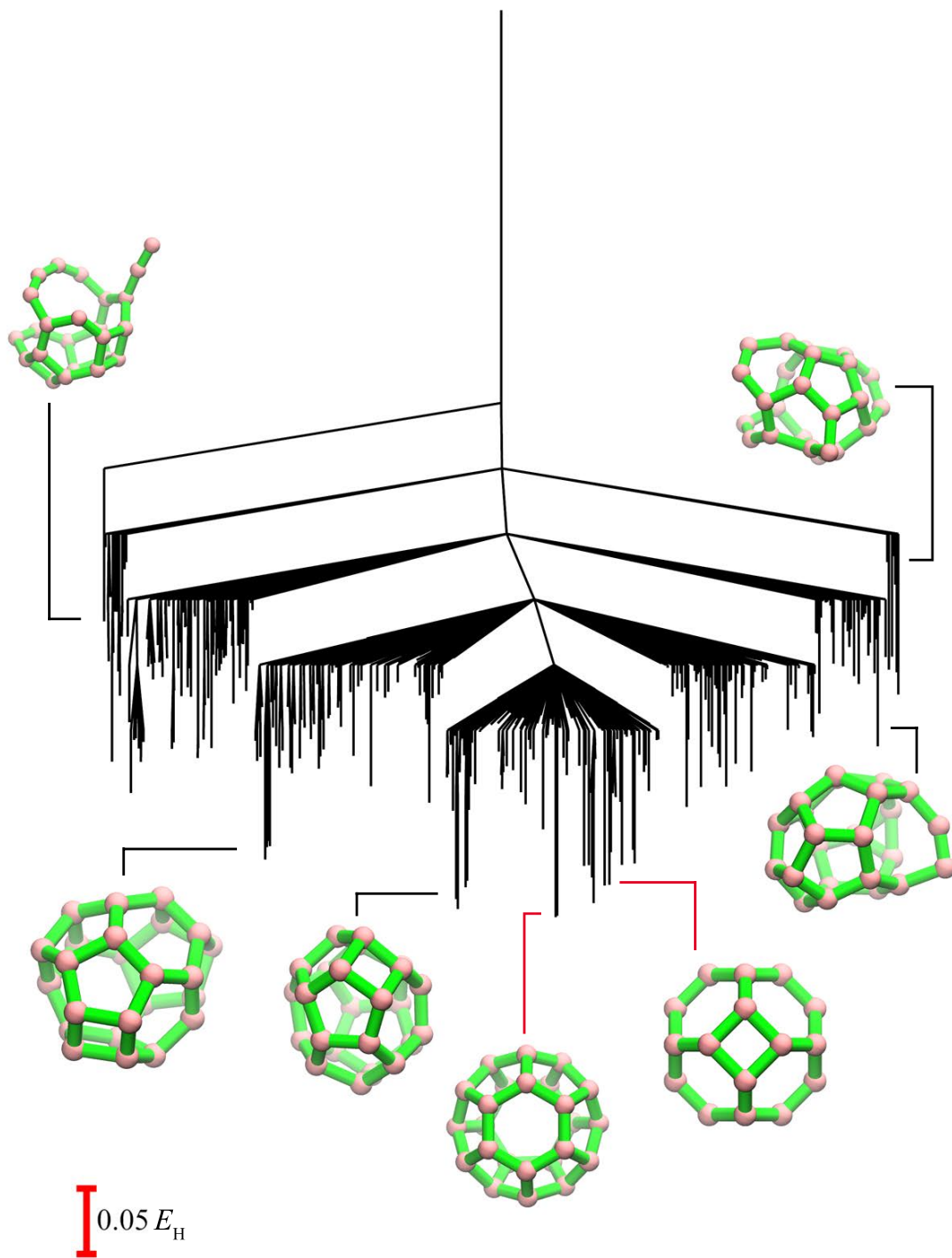


Figure 1: Disconnectivity graph^{45,46} for C_{24} with the SCC-DFTB potential. Red lines designate the endpoint minima for the initial pathway calculation and the scale bar defines the energy scale.

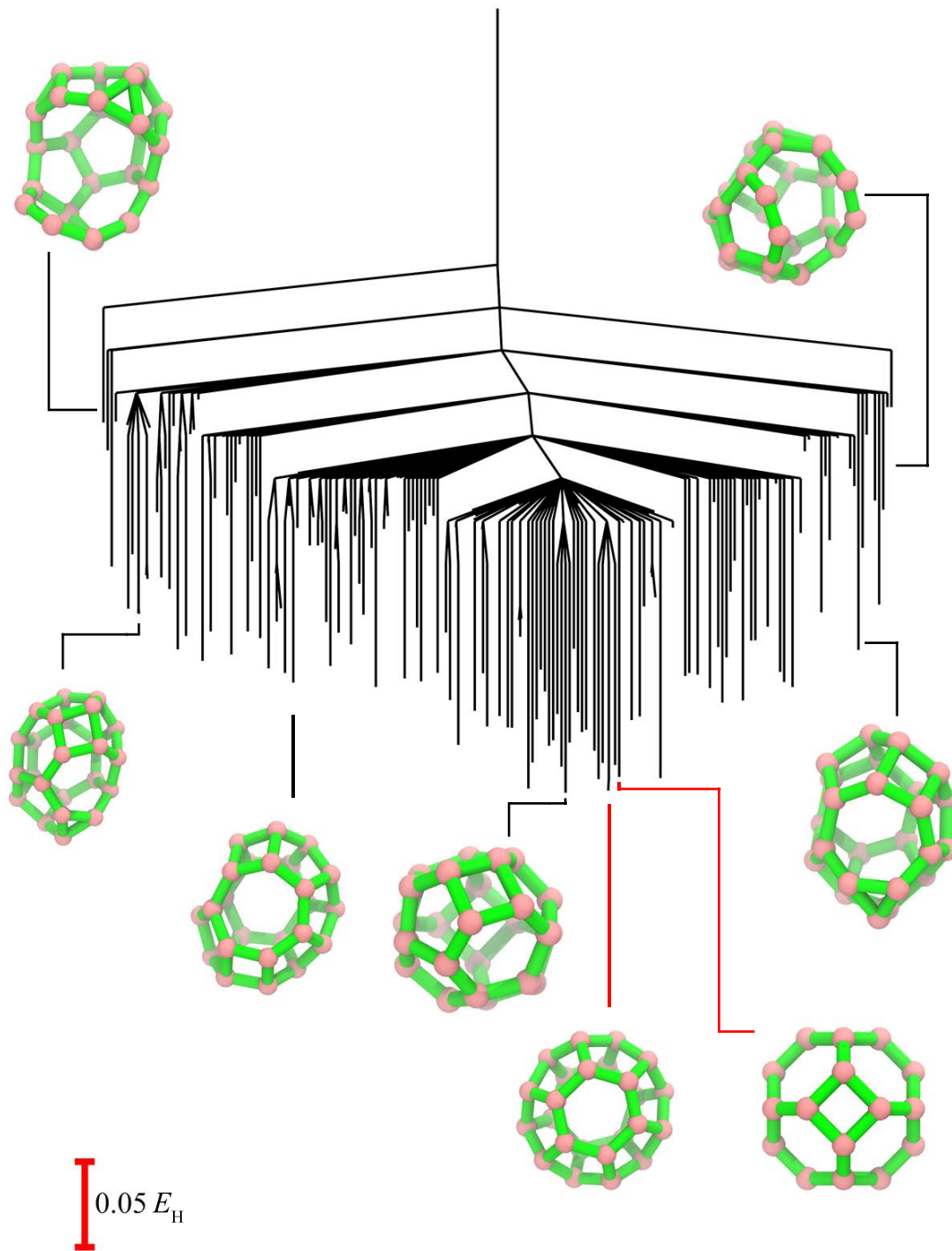


Figure 2: Disconnectivity graph^{45,46} for C₂₄ with the GFN2-xTB potential. Red lines designate the endpoint minima for the initial pathway calculation and the scale bar defines the energy scale.

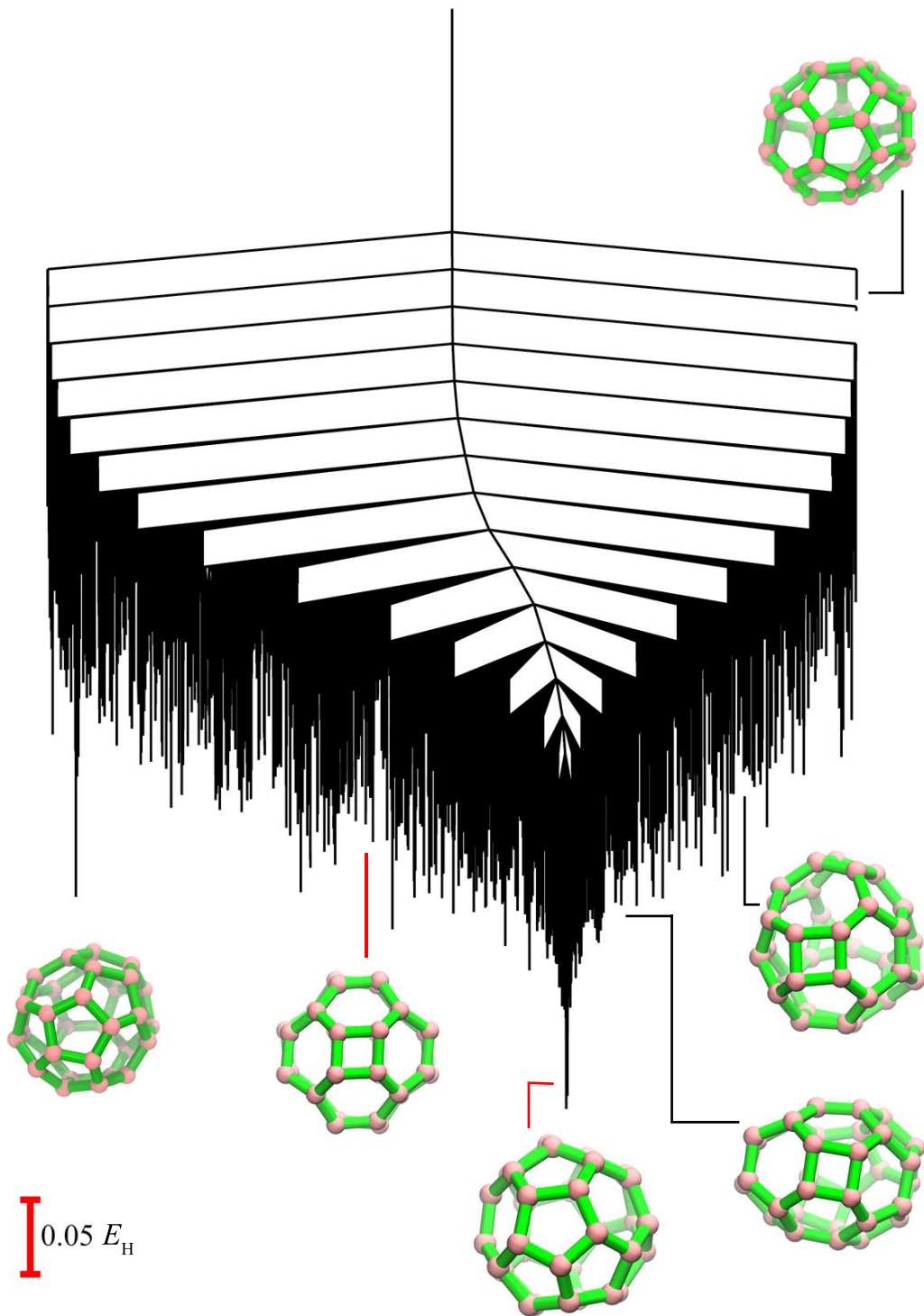


Figure 3: Disconnectivity graph^{45,46} for C₃₂ with the SCC-DFTB potential. Red lines designate the endpoint minima for the initial pathway calculation and the scale bar defines the energy scale.

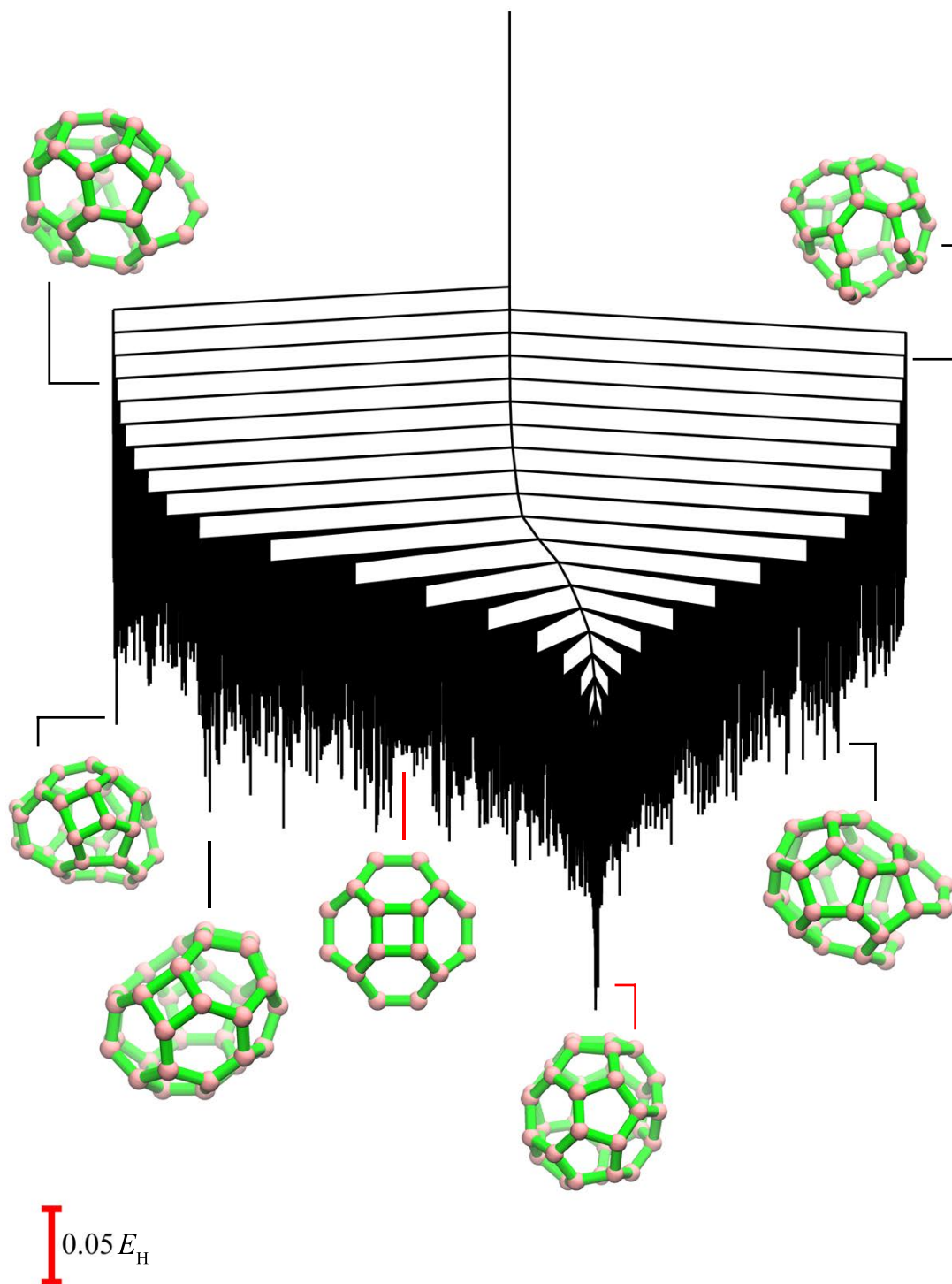


Figure 4: Disconnectivity graph^{45,46} for C₃₂ with the GFN2-xTB potential. Red lines designate the endpoint minima for the initial pathway calculation and the scale bar defines the energy scale.

Buckyball to Buckybowl

The largest system analysed in this study is C_{60} . From Figs. 5-6 we see that funneled organisation⁵²⁻⁵⁴ emerges for the energy landscape with both potentials. Previous studies with ab initio and tight-binding potentials have reported consistent results for the fullerene region of the graph.^{55,56} As expected, the buckyball is the most stable structure and lies at the bottom of the funnel. Judging from the energy gradient of the funnel, we expect that, given enough thermal energy and sufficient annealing time, the global minimum should be located easily, which confirms the previous studies of buckyball relaxation dynamics.^{55,56} Both potentials are also consistent with regard to the nature of the high-lying, less stable minima, including the bowl-shaped structure (the “buckybowl”). Unsurprisingly, the buckybowl lies at the top of the energy range, and is $1.264 E_h$ and $1.462 E_h$ above the fullerene global minimum for SCC-DFTB and GFN2-xTB, respectively. Both potentials show similar features, including the identity of the global minimum and the high-energy, cleaved fullerenes. The highest-lying structures generally correspond to buckybowls with one or more dangling chains. Such structures should be favoured by entropy under high-temperature conditions, and may also prevail in interstellar media²⁰ where they could provide a starting point for fullerene synthesis.

Mechanisms and Kinetics

Octahedral to Fullerene

To gain mechanistic insights into the transformation process from the octahedral to fullerene clusters, as well as from a buckybowl to the buckyball, Dijkstra’s shortest path algorithm⁵⁷ with suitable edge weights⁴¹ was used to extract pathways from the stationary point databases that make the largest contributions to the rate constant (i.e. the fastest path). We begin by analysing the mechanism for C_{24} , which is shown in Figs. 7a-7b. It involves three pericyclic local C_2 rotation rearrangements,⁵⁸ which transform the octahedral cluster into a fullerene. The three barriers are $0.163 E_h$, $0.134 E_h$ and $0.134 E_h$. The other potential, GFN2-xTB,

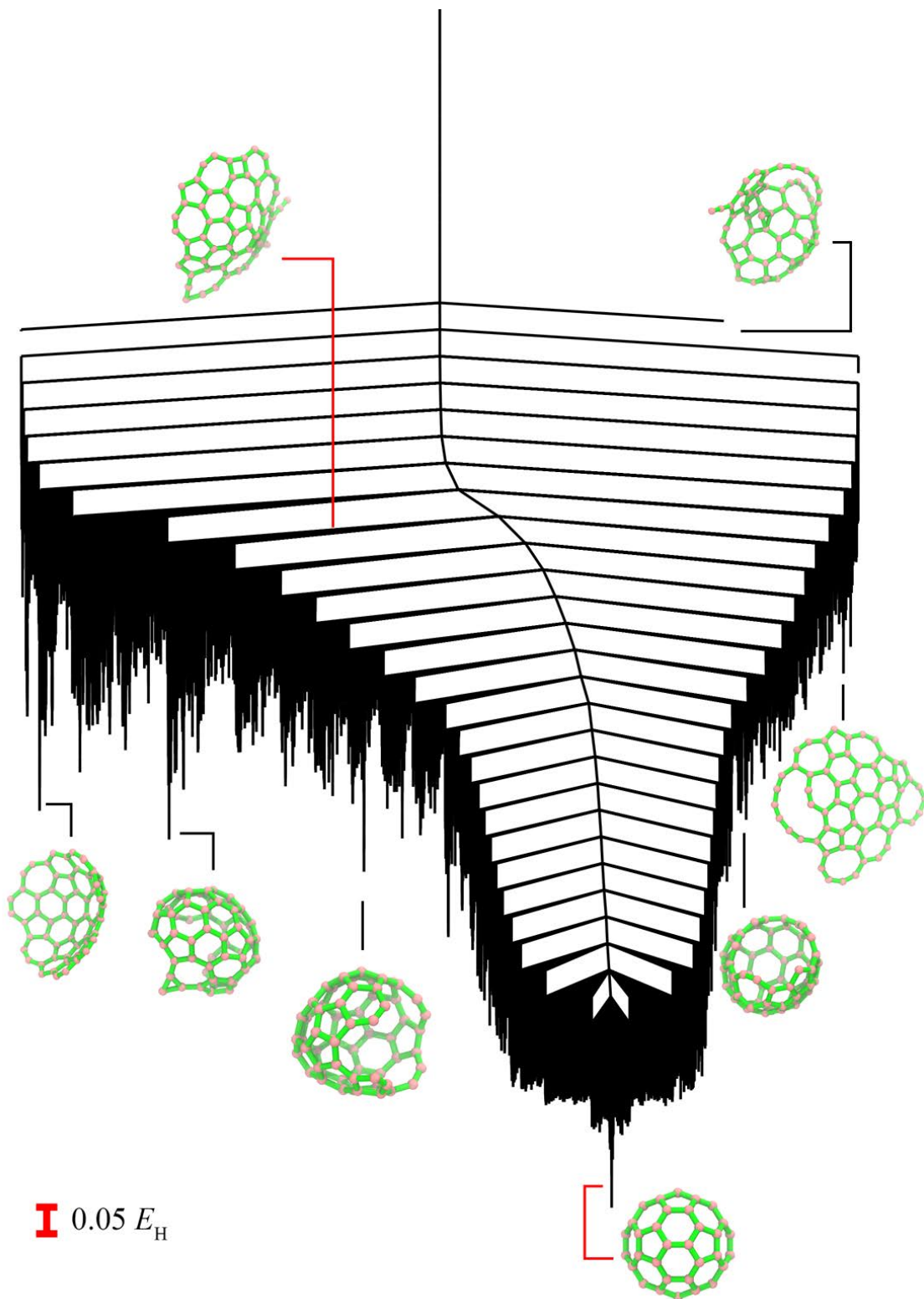


Figure 5: Disconnectivity graph^{45,46} for C₆₀ with the SCC-DFTB potential. Red lines designate the endpoint minima for the initial pathway calculation and the scale bar defines the energy scale.

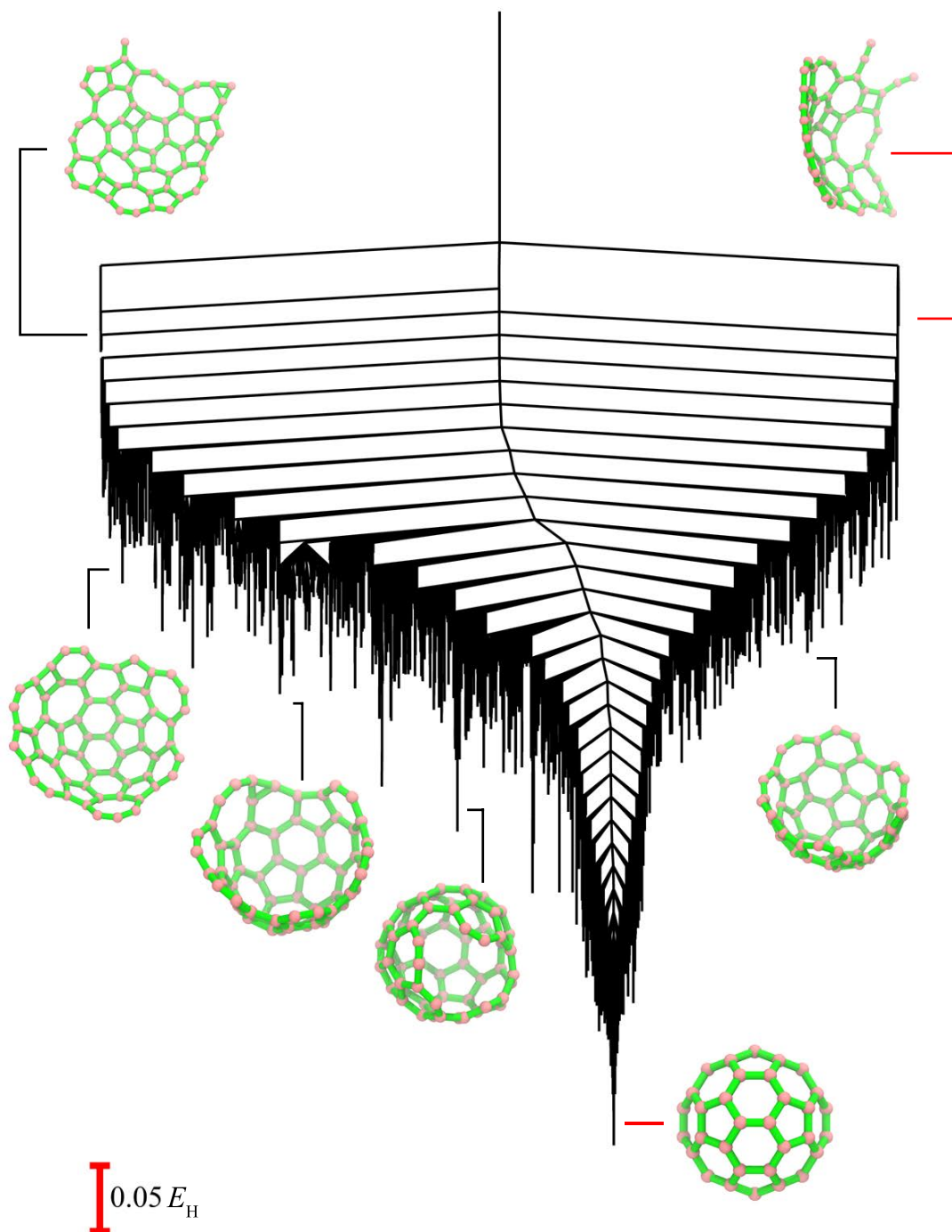


Figure 6: Disconnectivity graph^{45,46} for C_{60} with the GFN2-xTB potential. Red lines designate the endpoint minima and the scale bar defines the energy scale.

predicts a fastest path with three steps as well, but with somewhat larger barriers of $0.169 E_h$, $0.150 E_h$ and $0.138 E_h$. In the benchmark DFT (PBE/cc-pVTZ) calculations, the pathway is made up of three steps, with the following barriers: $0.168 E_h$, $0.144 E_h$ and $0.143 E_h$ for the final step. Hence, the root mean square errors for the barrier heights are $0.008 E_h$ and $0.005 E_h$ for SCC-DFTB and GFN2-xTB, respectively.

In contrast, the C_{32} pathway (Figures Figs. 8a-8b) is almost twice as long, and contains six basic rearrangements. Similar to the previous pathway, it is a downhill process regardless of the potential, but differs with respect to the barrier heights. For SCC-DFTB, the barriers are $0.150 E_h$, $0.146 E_h$, $0.147 E_h$, $0.122 E_h$, $0.195 E_h$ and $0.169 E_h$. In comparison, GFN2-xTB exhibits generally larger barriers for this system: $0.163 E_h$, $0.154 E_h$, $0.164 E_h$, $0.145 E_h$, $0.198 E_h$, and $0.182 E_h$. Although the numerical values differ, the overall trends between SCC-DFTB and GFN2-xTB agree. The pathway obtained from DFT (PBE/STO-3G) exhibits 13 steps with 8 key barriers (in the range of 0.15 - $0.25 E_h$) and 5 additional minor rearrangements with barriers of 0.001 - $0.07 E_h$. The extra five steps are a consequence of the initial DNEB interpolation, and would probably disappear from the fastest path with further refinement. For our purposes, the initial pathway is sufficient for benchmarking the energies and we did not refine it further. Single point calculations of the energies with a larger basis set (cc-pVTZ) of the previous pathway generally increased the barriers (up to $0.49 E_h$).

The overall rate constants for the transitions were computed from the databases using the graph transformation approach^{50,51} over a temperature range of 800-2000 K, employing the self-consistent regrouping scheme.⁴⁷ The regrouping procedure should remove bias arising due to the original choice of endpoints, by expanding single stationary points into ensembles of structures in local equilibrium at the chosen observation time scale. The kinetics are then described in terms of transitions between groups of minima. The estimated rate constants take into account all possible paths that exist between two reactant and product macrostates. Regrouping thresholds between 0.15 - $0.20 E_h$ were found appropriate for

these systems, as values in this range resulted in practically identical rates, indicating a well-defined organisation for the regrouped database.

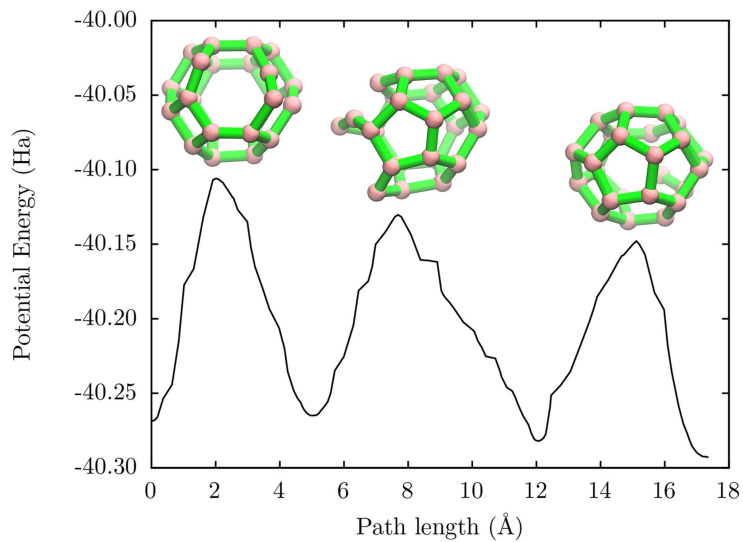
Inspection of Tables 1-2 reveals that both potentials predict the octahedral to fullerene route to be significantly faster than the reverse transition, in agreement with the overall downhill energy profile observed in Figs. 7a-7b. At the highest temperature (2000 K), the predicted fullerene formation timescales are on the order of 1 ms and 100 ms for SCC-DFTB and GFN2-xTB, respectively, for C_{24} . In the case of C_{32} , the disparity between potentials is even larger, with timescales of 2 ms and 3×10^4 ms. The much slower rates in the latter case probably result from the higher barriers exhibited by GFN2-xTB. Given the exponential sensitivity of rate constants to barrier heights these values should be considered as estimates, and it is probably more useful to compare the effective activation energies between the two potentials. From an Arrhenius analysis based on the rates, the effective activation energies for the forward and reverse C_{24} transformation were extracted, producing values for SCC-DFTB of $0.162 E_h$ and $0.173 E_h$, respectively. The same cluster exhibits Arrhenius activation energies of $0.167 E_h$ and $0.173 E_h$ with the GFN2-xTB potential. For the C_{32} transformation, the activation energies are $0.14 E_h$ and $0.19 E_h$ with SCC-DFTB, and $0.20 E_h$ and $0.39 E_h$ with GFN2-xTB.

Table 1: Rate constants (s^{-1}) for transitions between octahedral (O) and fullerene (F) structures of C_{24} using the SCC-DFTB (top two rows) and GFN2-xTB (bottom two rows) potentials.

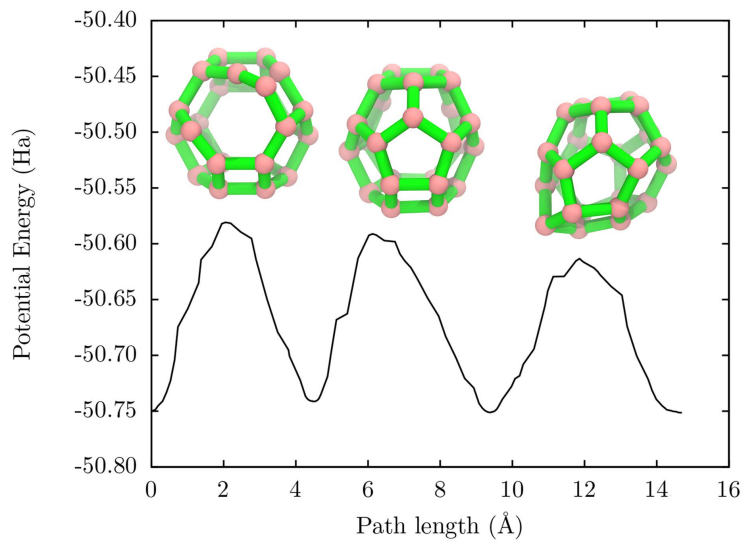
	800 K	1000 K	1500 K	2000 K
$O_{24} \rightarrow F_{24}$	2×10^{-14}	6×10^{-9}	2×10^{-1}	8×10^2
$F_{24} \rightarrow O_{24}$	7×10^{-20}	1×10^{-13}	4×10^{-5}	3×10^{-1}
$O_{24} \rightarrow F_{24}$	3×10^{-17}	2×10^{-11}	1×10^{-3}	8×10^0
$F_{24} \rightarrow O_{24}$	2×10^{-19}	2×10^{-13}	2×10^{-5}	2×10^{-1}

Buckyball to Buckybowl

Figs. 9a-9b present the fastest paths for the transformation process from a buckyball into a buckybowl. For these potentials the overall path length is similar and contains over 50



(a) SCC-DFTB

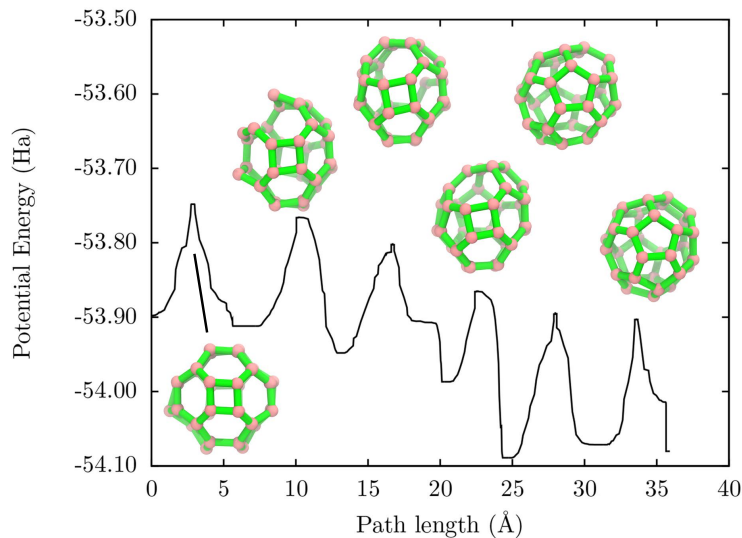


(b) GFN2-xTB

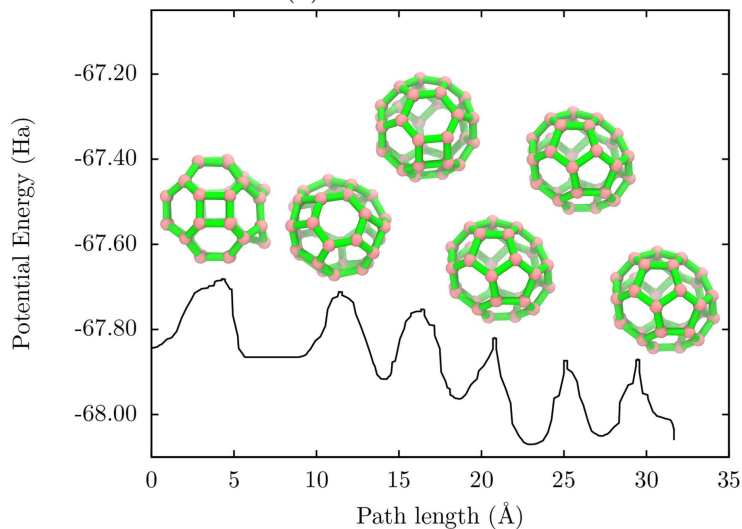
Figure 7: The potential energy as a function of the integrated path length for the pathway that makes the largest contribution to the overall rate constant for the octahedral to fullerene C_{24} transformation. Representative snapshots of the transition states along the pathway are also shown.

Table 2: Rate constants (s^{-1}) for transitions between octahedral (O) and fullerene (F) structures of C_{32} using the SCC-DFTB (top two rows) and GFN2-xTB (bottom two rows) potentials.

	800 K	1000 K	1500 K	2000 K
$O_{32} \rightarrow F_{32}$	1×10^{-12}	9×10^{-8}	3×10^{-1}	6×10^2
$F_{32} \rightarrow O_{32}$	1×10^{-19}	5×10^{-13}	3×10^{-4}	8×10^0
$O_{32} \rightarrow F_{32}$	3×10^{-23}	2×10^{-16}	7×10^{-7}	3×10^{-2}
$F_{32} \rightarrow O_{32}$	5×10^{-52}	1×10^{-38}	8×10^{-21}	6×10^{-12}



(a) SCC-DFTB



(b) GFN2-xTB

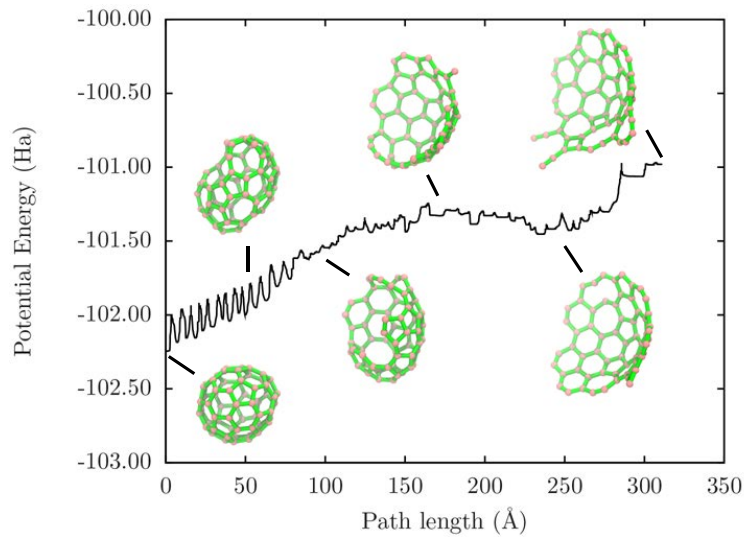
Figure 8: The potential energy as a function of the integrated path length for the pathway that makes the largest contribution to the overall rate constant for the octahedral to fullerene C_{32} transformation. Representative snapshots of the transition states along the pathway are also shown.

transition states that link the two endpoints. The potential energy profile reveals three common trends: (a) the first region (30-70 Å) is characterised by a steeply increasing profile with rather high barriers; before the emergence of a (b) wide intermediate region where the energy profile plateaus; and then (c) a steeper rise in energy is seen again (final 20 Å) where the bowl-shaped endpoint is finally reached. A close inspection of the energy barriers reveals that the process begins with well-defined pericyclic local C_2 rearrangements and associated barriers of $0.18 E_h$ and $0.20 E_h$ for GFN2-xTB and SCC-DFTB, respectively. After several such steps, the potential energy quickly increases and the cluster begins to lose its spherical structure together with the introduction of triangular rings. Further small rearrangements cleave the cluster completely and several dangling carbon chains appear. These chains increase the potential energy of the bowl-shaped structure, and as discussed in the following section, also contribute to a significant increase in entropy.

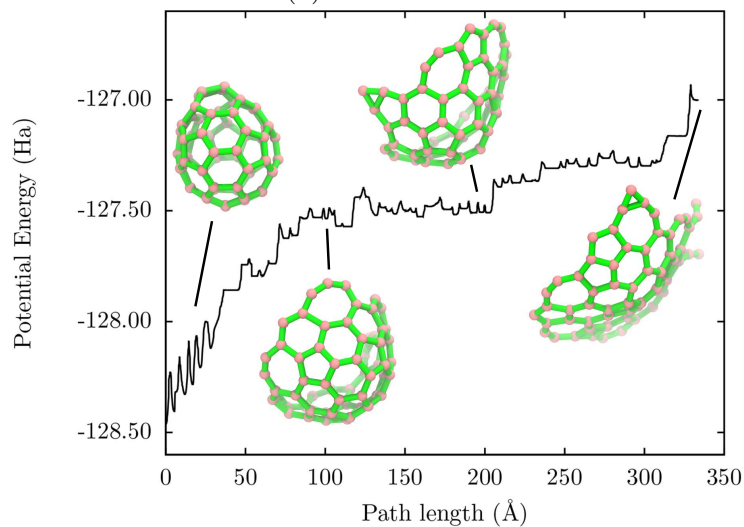
Table 3: Rate constants (s^{-1}) for transitions between buckybowl and buckyball structures using the SCC-DFTB (top two rows) and GFN2-xTB (bottom two rows) potentials.

	2000 K	3000 K	4000 K	5000 K
bowl \rightarrow ball	4×10^{-1}	5×10^5	8×10^6	3×10^3
ball \rightarrow bowl	8×10^{-3}	2×10^0	2×10^3	7×10^4
bowl \rightarrow ball	1×10^{-7}	9×10^{-2}	7×10^{-1}	3×10^3
ball \rightarrow bowl	3×10^{-69}	3×10^{-34}	5×10^{-17}	5×10^{-7}

As above, the overall rate constants for the transformation were computed using graph transformation^{50,51} coupled with the self-consistent regrouping scheme.⁴⁷ Due to the larger barriers we have calculated the rate constants at a higher range of temperatures, namely 2000-5000 K, corresponding to relevant transformation timescales. In agreement with the larger barriers encountered in the GFN2-xTB pathway, the rate constants for the transformation are several orders of magnitude smaller compared to the SCC-DFTB pathway. For example, the overall largest barriers in the ball to bowl and bowl to ball directions using GFN2-xTB are $1.53 E_h$ and $0.07 E_h$, while the respective barriers using SCC-DFTB are $1.27 E_h$ and $0.01 E_h$, respectively. According to Table 3, the ball to bowl rates in the case of SCC-DFTB show an unexpected decrease with increasing temperature. Moreover, a turning



(a) SCC-DFTB



(b) GFN2-xTB

Figure 9: The potential energy as a function of the integrated path length for the pathway that makes the largest contribution to the rate constant for the buckyball to buckybowl transformation. Representative snapshots of the structures along the pathway are also shown.

point at around 4500 K exists where the typical Arrhenius behaviour breaks down, and the rate starts to decrease with a further increase in temperature. This behaviour occurs for both potentials, albeit at a higher temperature for GFN2-xTB (around 6000 K).

Origin of the Rate Maximum

To understand the origin of the rate maximum we reduced the kinetic scheme to a simple analytical model that exhibits the same behaviour. Consider a three-state system with minima A , I and B , where A and B are the endpoints and I is an intervening structure. Transition states $ts1$ and $ts2$ connect A and I , and I and B , respectively, with associated minimum-to-minimum rate constants k_{IB} for $B \rightarrow I$, etc. For specificity, we focus on the transformation rate $B \rightarrow A$. The mean first-passage time for trajectories starting in B and eventually arriving at A for the first time⁵⁹ (MFPT) is analytical⁵⁰ and given by Eq. (1)

$$\mathcal{T}_{AB} = \frac{P_{IB}P_{AI}(\tau_I + \tau_B)}{(1 - P_{IB}P_{BI})^2} \quad (1)$$

where P_{IB} , P_{AI} , and P_{BI} are the branching probabilities from B to I , I to A and I to B , and τ_I and τ_B are the waiting times for transitions out of I and B . For this simple system $P_{IB} = 1$, $P_{AI} = k_{AI}/(k_{AI} + k_{BI})$, $P_{BI} = k_{BI}/(k_{AI} + k_{BI})$, $\tau_I = 1/(k_{AI} + k_{BI})$ and $\tau_B = 1/k_{IB}$.

The mean number of steps (MNS, the dynamic activity,⁶⁰ \mathcal{S}_{AB}) is the same as the MFPT except that the $(\tau_I + \tau_B)$ term becomes 2, and is given by Eq. (2)

$$\mathcal{S}_{AB} = \frac{2P_{IB}P_{AI}}{(1 - P_{IB}P_{BI})^2}. \quad (2)$$

Substituting the elementary rate constants into the branching probabilities and waiting times gives Eq. (3)

$$\mathcal{T}_{AB} = \frac{k_{IB} + k_{AI} + k_{BI}}{k_{IB}k_{AI}} \quad (3)$$

and similarly, the MNS simplifies to

$$\mathcal{S}_{AB} = \frac{2(k_{AI} + k_{BI})}{k_{AI}}. \quad (4)$$

To illustrate the turnover effect, we now use Transition State Theory^{48,49} for the minimum-to-minimum rate constants written as:

$$\begin{aligned} \ln k_{IB} &= \ln[o_B/(2\pi o_{ts2})] + (\Lambda_B - \Lambda_{ts2})/2 - (E^{ts2} - E^B)/k_B T, \\ \ln k_{AI} &= \ln[o_I/(2\pi o_{ts1})] + (\Lambda_I - \Lambda_{ts1})/2 - (E^{ts1} - E^I)/k_B T, \\ \ln k_{BI} &= \ln[o_I/(2\pi o_{ts2})] + (\Lambda_I - \Lambda_{ts2})/2 - (E^{ts2} - E^I)/k_B T. \end{aligned} \quad (5)$$

The symmetry factors o_α were all set to unity. Λ is the natural log of the product of positive mass-weighted Hessian eigenvalues, and the factor of 2π arises from conversion of an angular normal mode frequency because there is one fewer positive Hessian eigenvalue for the transition states. Each positive Hessian eigenvalue is associated with the square of an angular normal mode frequency, which is accounted for by the factors of 2. This formulation assumes a harmonic normal mode approximation for the vibrational density of states. Finally, the potential energies of the stationary points are E^A , E^{ts1} , etc.

The turnover effect arises for suitable choices of the vibrational terms and energies. Here we illustrate some numerical results for $E^{ts1} = 1$, $E^{ts2} = 2$, $E^B = 1.5$, $E^I = 0$, $\Lambda_B = 10$, $\Lambda_{ts1} = 30$, $\Lambda_{ts2} = 0$, $\Lambda_I = 50$ and set the Boltzmann constant $k_B = 1$ so that temperature is in the same arbitrary units as the potential energy. These values simplify the more complex network of the buckyball system, but retain the essential physics that can produce a rate turnover. The terms $-\Lambda$ correspond to vibrational entropy, and in this scenario the starting minimum B and the transition state $ts2$ have significantly higher entropies than the intervening minimum, I , and the transition state connecting I to product A . In the buckyball pathway, the high energy minima and transition states with bowl structures can have low-coordinate dangling carbon atoms, with associated low frequency vibrational modes, and

hence large vibrational entropies.

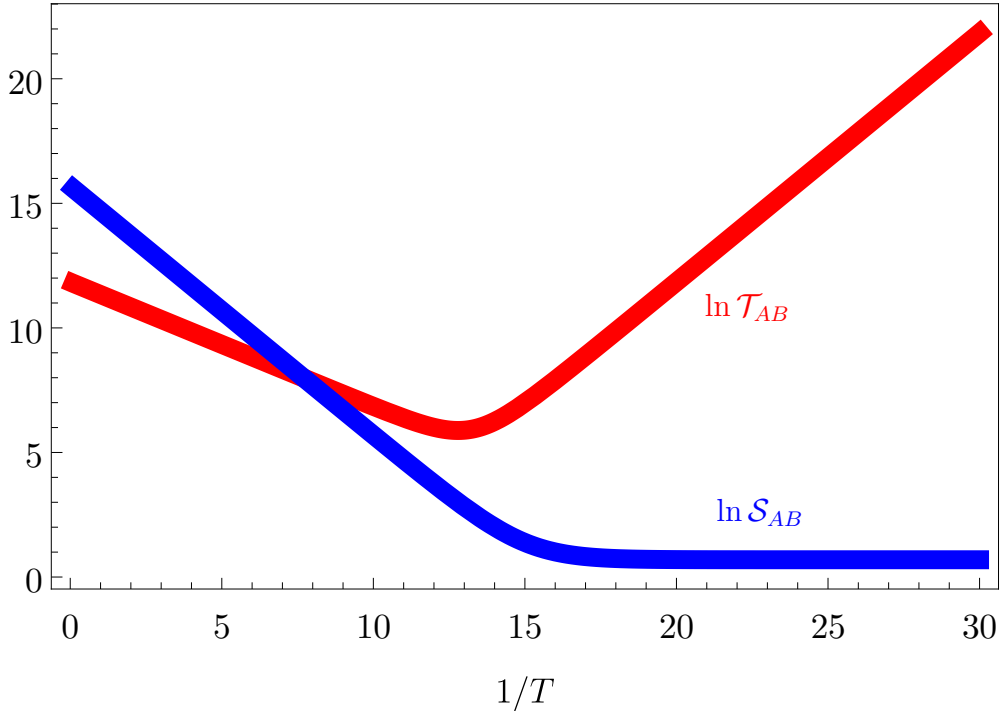


Figure 10: Plot of the mean first-passage time (MFPT, $\ln \mathcal{T}_{AB}$) and mean number of steps (MNS, $\ln \mathcal{S}_{AB}$) for $B \rightarrow A$ transitions in a model three-state system as a function of inverse temperature. The minimum in the MFPT corresponds to a maximum in the rate.

$\ln \mathcal{T}_{AB}$ and $\ln \mathcal{S}_{AB}$ are plotted as a function of $1/T$ in Figure 10. This kinetic system exhibits a minimum in the MFPT, which translates to a maximum for the overall rate, while the MNS reaches a plateau in the limit of low temperature. Examining the contributions of the three terms in equation (3) explains this behaviour. The first two terms are inverse rate constants, which always increase as T decreases. The third term $k_{BI}/(k_{IB}k_{AI})$ is small at low temperature, but grows rapidly at high temperature. In the high temperature limit, the energetic barriers are irrelevant, and trajectories revisit B from I many times because B is favoured by entropy. This effect is also reflected in the growth of $\ln \mathcal{S}_{AB}$ as the temperature increases in Figure 10. \mathcal{S}_{AB} can be written as $2/P_{AI} = 2/(1 - P_{BI})$, and grows rapidly in the high temperature limit if return to B is much more likely than a transition to product. In the low temperature limit, the MFPT increases with $1/T$ because the $I \rightarrow A$ transition is slow.

The ratio $k_{BI}/(k_{IB}k_{AI})$ can exhibit a turnover with increasing T when Λ_B is smaller than Λ_{ts1} , i.e. the vibrational entropy of the starting high-energy minimum is larger than for $ts1$. We emphasise that these interpretations do not depend upon the validity of transition state theory, which is used here for specificity, and is not expected to be particularly accurate at high temperature. The point is, that if such a kinetic scheme applies, then the interplay of entropy and potential energy can produce a maximum in the overall rate. This scenario is unusual, but the high-entropy bowl structures with weakly bound peripheral carbon atoms may provide an example with practical implications. We note that this behaviour is different from more familiar deviations from Arrhenius kinetics (for example due to tunneling at low temperatures).⁶¹

Infrared Spectra

The IR spectra were calculated at the DFT (PBE0/cc-pVDZ) level. This approach was tested previously for C_8H_8 cubane⁶² and reproduced the experimental IR band positions and relative intensities very well (with deviations within 5%), especially the low-frequency modes dominated by the carbon skeleton. Fig. 11 shows the spectra for fullerene (f) and octahedral (o) structures of C_{24} and C_{32} within the range 400 to 1600 cm^{-1} .

For both C_{24} and C_{32} , a characteristic feature is the higher (T_{1u}) degeneracy of lines for the $C_n(o)$ isomers, which makes their spectra notably sparser. All the spectra are comparably bright, except for $C_{24}(f)$ with its rather unique line near 540 cm^{-1} , which is an order of magnitude more intense (and non-degenerate). In particular, the predicted structure of the $C_{24}(f)$ spectrum is similar to that calculated previously.⁶³ Four secondary lines of $C_{24}(f)$ (near 600, 960, 1320, and 860 cm^{-1}) are doublets, while the three most intense lines of $C_{32}(f)$ (near 1270, 700, and 1440 cm^{-1}) correspond to non-degenerate modes. In addition, the C_{32} cluster shows an overall redistribution of intensity from lower to higher frequencies upon the octahedral-to-fullerene transition, unlike the C_{24} counterpart. In particular, the primary line of $C_{24}(f)$ near 540 cm^{-1} corresponds to a bending mode with radial stretch of C_{12} bowl-halves

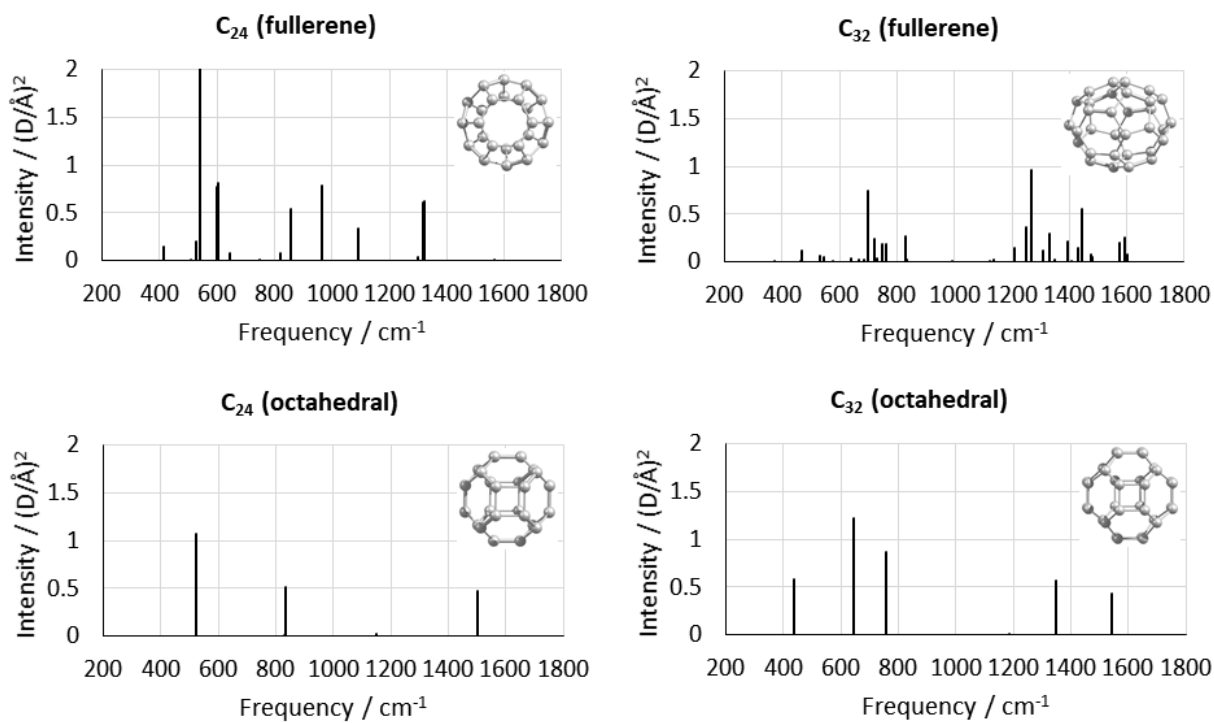


Figure 11: Calculated IR spectra of C₂₄ and C₃₂ clusters. Note: for C₂₄ (fullerene) the line near 540 cm⁻¹ has intensity 8.1 (D/Å)², and is cut off so that the other features are discernible.

in counter-phase. In other words, all C_2 -links of the central 12-atom (zigzagged) belt rock, so that the two staggered six-atom rings stretch and shrink in counter-phase. As a result, a strong variation of dipole moment occurs along the symmetry axis, oscillating between opposite directions, leading to high intensity. In comparison, the brightest line of $C_{24}(o)$ near 520 cm^{-1} involves a similar radial stretch of only the C_8 bowls capping the central C_8 ring. This ring is essentially a spectator, and remains almost frozen, in contrast to the situation for $C_{24}(f)$. This structure can be related to the significantly smaller variation of the dipole moment, resulting in a lower intensity.

Interestingly, the most intense line of $C_{32}(o)$ near 650 cm^{-1} corresponds to a vibration combining the C_8 -bowl radial stretch found in $C_{24}(o)$ and rocking of the central C_{16} (double C_8 -ring) belt, analogous to the motion exhibited by $C_{24}(f)$. This rocking moves the belt atoms, unlike those of the (almost frozen) central C_8 ring of $C_{24}(o)$, which could be viewed as a larger effective mass for the ring atoms, resulting in the lower frequency for $C_{24}(o)$. In addition, the rocking in $C_{32}(o)$ shifts the belt atoms in counter-phase with the capping-bowl atoms, which can in part cancel their contributions to the asymmetry-induced dipole-moment, and thus lowers the line intensity relative to that for $C_{24}(f)$, where the similar radial stretch and rocking involve the same atoms (and are thus in phase).

Ionic Derivatives and Reactivities

Upon ionization or electron attachment both fullerene and octahedral C_n are predicted to preserve their shapes for both $n=24$ and 32 . The corresponding energies (including vertical ones) calculated at the PBE0/cc-pVTZ level are collected in Table 4. The relaxation energies of the ions (i.e. $VIE - IE$ and $EA - VEA$) fall within about $0.1\text{-}0.2\text{ eV}$ for all species except $C_{24}(o)$, which reaches 0.5 eV . C_{32} exhibits both largest and smallest (V)IE values for the fullerene and octahedral species, respectively, with a drop of about 1.5 eV for the latter, while the C_{24} counterparts have a much smaller variation in the opposite direction. For $C_n(f)$ the (V)IE values increase with size, but decrease for $C_n(o)$. The (V)EA values decrease from

the fullerenes to the octahedral clusters for both sizes, more strongly for C_{24} . Curiously, unlike the octahedral clusters where (V)EA increases with size, the fullerenes show almost no alteration.

Table 4: Vertical and adiabatic ionization energies and electron affinities and reactivity parameters (chemical potential, hardness, electrophilicity), all in eV.

System	VIE	IE	VEA	EA	μ	η	ω
F_{24}	7.60	7.40	2.60	2.79	-5.10	2.30	5.65
O_{24}	7.83	7.75	1.85	2.32	-5.03	2.71	4.66
F_{32}	8.11	7.98	2.56	2.79	-5.39	2.60	5.60
O_{32}	6.66	6.57	2.42	2.58	-4.57	2.00	5.23

Specific combinations of the IE and EA values represent overall reactivity parameters such as chemical potential, $\mu \simeq -(IE + EA)/2$, and hardness, $\eta = (IE - EA)/2$, related to electronegativity and polarisability, respectively, as well as electrophilicity, $\omega = \mu^2/(2\eta)$,^{64,65} also listed in Table 4. The μ values are found to be higher for $C_n(o)$, especially for C_{32} , and increase with size for the octahedral clusters, while increasing for the fullerenes. The ω values are lower for $C_n(o)$, especially for C_{24} , and increase with size for the octahedral clusters, while remaining similar for the fullerenes.

Mechanistic Implications for Cosmic Buckyballs

The majority of cosmic fullerene detections arise in various types of evolved stars.³ At low temperatures, condensation favours production of a variety of small carbon molecules. Above 1000 K, the nature of the possible chemical reactions changes, and a whole family of polycyclic aromatic hydrocarbon (PAH) molecules can be synthesised.²³ Buckyballs can be formed at high temperatures as well (above 3500 K), where the competing production of PAHs is suppressed, and condensation begins in a bottom-up fashion. Intermediates, such as bowl-shaped clusters with side chains are first formed from simple diatomic and other small carbon molecules, and fold to produce the basic skeleton of a buckyball.^{21,23} Such conditions are expected in supernovae⁶⁶ or in the hot circumstellar dust environments of carbon-rich

stars, such as Wolf-Rayet stars.⁶⁷

Interestingly, it has recently been proposed that interstellar PAHs can also provide a top-down formation route, which again involves a bowl-shaped intermediate, resulting in generation of buckyballs under UV irradiation in low density and temperature regions.⁶⁸ Thus, it seems that buckybowls may play a role in the formation of buckyballs regardless of the specific mechanism. In this regard, the identification of an upper temperature limit of around 5250 K (for the two potentials), above which the formation rate of buckyballs from buckybowls diminishes due to associated entropic effects, might allow us to narrow down the possible scenarios and zones in which significant synthesis takes place. Thus, the optimal temperature range for a significant cosmic buckyball production may lie between around 3500 to 5250 K.

Summary

A new class of octahedral carbon clusters has recently been computationally predicted to have significant stability compared to fullerenes. Although the buckyball has been well characterised, its formation mechanisms remain elusive. Using Energy Landscape Theory and tight-binding potentials (SCC-DFTB and GFN2-xTB), we have calculated complete transformation pathways between octahedral 24-atom and 32-atom carbon clusters and the respective fullerenes, and between a buckyball and a buckybowl, a key intermediate, which appears in both top-down and bottom-up pathways to a buckyball.

Our results suggest that the overall energy landscapes in such cases are relatively funneled, so that transformation from any high-energy structure to the global minimum (fullerene isomer) should be achieved easily, provided that enough thermal energy is available. From a mechanistic viewpoint, the transformation from octahedral cluster to fullerene occurs through a series of pericyclic local C_2 rearrangements. In the case of C_{24} , the fastest path involves three steps, while for the C_{32} system there are six. The predicted IR spectra clearly

track the transformation between the fullerene and octahedral isomers of C_{24} and C_{32} in terms of a reduction in the number of different (triply degenerate) lines for the O_h -symmetric species. Analysis of the corresponding vibrations provides an interpretation for the relative IR intensities, including the uniquely bright line for the C_{24} fullerene cluster. The most intense lines are associated with the shape-distortion induced dipole moment oscillating in opposite directions along the symmetry axis.

We find that although the numerical values for the energy barriers differ, the overall trends between the two tight-binding potentials are consistent. With regard to computation timings, SCC-DFTB is faster by a factor of 1.5-2 compared to GFN2-xTB, which is somewhat expected as the latter includes multipole electrostatics and a DFT-D4 dispersion. predict the octahedral to fullerene route to be significantly faster than the reverse transition. In the case of C_{60} , the overall path between a buckyball and a buckybowl contains over 50 transition states, which again begin with basic C_2 rearrangements. After several such steps, the potential energy quickly increases and the cluster begins to lose its spherical structure together with the introduction of triangular rings. Further small rearrangements cleave the cluster completely and several dangling carbon chains appear.

Surprisingly, the estimated transformation rate from a buckybowl to a buckyball has a maximum near 4500 K for SCC-DFTB and 6000 K for GFN2-xTB, after which the rate decreases with increasing temperature. From analysis of the results, and based on a simple analytical model, we find that this behaviour originates from the high vibrational entropy of the buckybowl endpoint. A reduced model shows that a turnover in the rate can appear if the vibrational entropy of the starting high-energy minimum exceeds that of the transition state leading to product. Although this behaviour corresponds to an idealised kinetic model, it may be useful in the search and characterisation efforts for interstellar fullerenes. Experimentally, it has been shown that fullerene formation via a condensation route occurs above 3500 K. The kinetic transition networks that we have characterised suggest that an upper bound for the rate appears around 5250 K, above which the formation rate of buckyball from buckybowl

decreases with temperature.

Acknowledgement

D.F. is grateful to the Herchel Smith Fund and Darwin College at the University of Cambridge for independent research fellowships. D.J.W. is grateful to the EPSRC for financial support under grant EP/N035003/1. The authors thank the Grimme research group for assistance with the GFN2-xTB code and Prof. S. M. Woodley for providing the initial C₂₄ and C₃₂ octahedral and fullerene optimised geometries.

Supporting Information Available

Input files for all types of calculations, additional low-energy minima for C₂₄ using the GFN2-xTB potential, movies of all transformation pathways as visualised by the fastest paths.

This material is available free of charge via the Internet at <http://pubs.acs.org/>.

References

- (1) Speranza, G. *Nanomaterials* **2021**, *11*, 967.
- (2) Lazauskas, T.; Sokol, A. A.; Woodley, S. M. *Nanoscale Adv.* **2019**, *1*, 89–93.
- (3) Woods, P. *Nat. Astron.* **2020**, *4*, 299–305.
- (4) Candian, A.; Gomes Rachid, M.; MacIsaac, H.; Staroverov, V. N.; Peeters, E.; Cami, J. *Mon. Notices Royal Astron. Soc.* **2019**, *485*, 1137–1146.
- (5) Dubosq, C.; Falvo, C.; Calvo, F.; Rapacioli, M.; Parneix, P.; Pino, T.; Simon, A. *Astron. Astrophys.* **2019**, *625*, L11.
- (6) Smalley, R. *Acc. Chem. Res.* **1992**, *25*, 98–105.
- (7) Kroto, H.; McKay, K. *Nature* **1988**, *331*, 328–331.

- (8) Heath, J. R. *Fullerenes*; Chapter 1, pp 1–23.
- (9) Hunter, J. M.; Fye, J. L.; Roskamp, E. J.; Jarrold, M. F. *J. Phys. Chem.* **1994**, *98*, 1810–1818.
- (10) Huang, J.; Ding, F.; Jiao, K.; Yakobson, B. I. *Phys. Rev. Lett.* **2007**, *99*, 175503.
- (11) Yannoni, C. S.; Bernier, P. P.; Bethune, D. S.; Meijer, G.; Salem, J. R. *J. Am. Chem. Soc.* **1991**, *113*, 3190–3192.
- (12) Hawkins, J. M.; Meyer, A.; Loren, S.; Nunlist, R. *J. Am. Chem. Soc.* **1991**, *113*, 9394–9395.
- (13) Ebbesen, T. W.; Tabuchi, J.; Tanigaki, K. *Chem. Phys. Lett.* **1992**, *191*, 336–338.
- (14) Scuseria, G. E. *Science* **1996**, *271*, 942–945.
- (15) Murry, R. L.; Scuseria, G. E. *Science* **1994**, *263*, 791–793.
- (16) Sure, R.; Hansen, A.; Schwerdtfeger, P.; Grimme, S. *Phys. Chem. Chem. Phys.* **2017**, *19*, 14296–14305.
- (17) Karton, A.; Waite, S. L.; Page, A. J. *J. Phys. Chem. A* **2019**, *123*, 257–266.
- (18) Chuvilin, A.; Kaiser, U.; Bichoutskaia, E.; Besley, N. A.; Khlobystov, A. N. *Nat. Chem.* **2010**, *2*, 450–453.
- (19) Zhang, J.; Bowles, F. L.; Bearden, D. W.; Ray, W. K.; Fuhrer, T.; Ye, Y.; Dixon, C.; Harich, K.; Helm, R. F.; Olmstead, M. M.; Balch, A. L.; Dorn, H. C. *Nat. Chem.* **2013**, *5*, 880–885.
- (20) Berné, O.; Montillaud, J.; Joblin, C. *Astron. Astrophys.* **2015**, *577*, A133.
- (21) Irle, S.; Zheng, G.; Elstner, M.; Morokuma, K. *Nano Letters* **2003**, *3*, 1657–1664.

- (22) Cami, J.; Peeters, E.; Bernard-Salas, J.; Doppmann, G.; De Buizer, J. *Galaxies* **2018**, *6*.
- (23) Jäger, C.; Huisken, F.; Mutschke, H.; Jansa, I. L.; Henning, T. *Astrophys. J.* **2009**, *696*, 706.
- (24) Micelotta, E. R.; Jones, A. P.; Cami, J.; Peeters, E.; Bernard-Salas, J.; Fanchini, G. *Astrophys. J.* **2012**, *761*, 35.
- (25) Wales, D. J. *Energy landscapes*, Cambridge molecular science. 2003.
- (26) Hourahine, B. et al. *J. Chem. Phys.* **2020**, *152*, 124101.
- (27) OPTIM: A program for geometry optimisation and pathway calculations. <http://www-wales.ch.cam.ac.uk/software.html> (accessed: July, 2021).
- (28) PATHSAMPLE: A program for generating connected stationary point databases and extracting global kinetics. <http://www-wales.ch.cam.ac.uk/software.html> (accessed: July, 2021).
- (29) Gaus, M.; Cui, Q.; Elstner, M. *J. Chem. Theory Comput.* **2011**, *7*, 931–948.
- (30) Gaus, M.; Goez, A.; Elstner, M. *J. Chem. Theory Comput.* **2013**, *9*, 338–354.
- (31) Bannwarth, C.; Ehlert, S.; Grimme, S. *J. Chem. Theory Comput.* **2019**, *15*, 1652–1671.
- (32) Frisch, M. J. et al. *Gaussian 09 Revision E.01*. Gaussian Inc. Wallingford CT 2009.
- (33) Trygubenko, S. A.; Wales, D. J. *J. Chem. Phys.* **2004**, *120*, 2082–2094.
- (34) Sheppard, D.; Terrell, R.; Henkelman, G. *J. Chem. Phys.* **2008**, *128*, 134106.
- (35) Jónsson, H.; Mills, G.; Jacobsen, K. W. *Classical and Quantum Dynamics in Condensed Phase Simulations*; pp 385–404.
- (36) Henkelman, G.; Jónsson, H. *J. Chem. Phys.* **2000**, *113*, 9978–9985.

- (37) Munro, L. J.; Wales, D. J. *Phys. Rev. B* **1999**, *59*, 3969–3980.
- (38) Henkelman, G.; Jónsson, H. *J. Chem. Phys.* **1999**, *111*, 7010–7022.
- (39) Kumeda, Y.; Munro, L. J.; Wales, D. J. *Chem. Phys. Lett.* **2001**, *341*, 185–194.
- (40) Zeng, Y.; Xiao, P.; Henkelman, G. *J. Chem. Phys.* **2014**, *140*, 044115.
- (41) Carr, J. M.; Trygubenko, S. A.; Wales, D. J. *J. Chem. Phys.* **2005**, *122*, 234903.
- (42) Strodel, B.; Whittleston, C. S.; Wales, D. J. *J. Amer. Chem. Soc.* **2007**, *129*, 16005–16014.
- (43) Wales, D. J.; Carr, J. M.; Khalili, M.; de Souza, V. K.; Strodel, B.; Whittleston, C. S. *Proteins: Energy, Heat and Signal Flow*; Computation in chemistry; CRC Press, 2009; p 315.
- (44) Wales, D. J. *Philos. Trans. R. Soc. A* **2012**, *370*, 2877–2899.
- (45) Becker, O. M.; Karplus, M. *J. Chem. Phys.* **1997**, *106*, 1495–1517.
- (46) Wales, D. J.; Miller, M. A.; Walsh, T. R. *Nature* **1998**, *394*, 758–760.
- (47) Carr, J. M.; Wales, D. J. *J. Phys. Chem. B* **2008**, *112*, 8760–8769.
- (48) Forst, W. *Theory of Unimolecular Reactions*; Academic Press: New York, 1973.
- (49) Laidler, K. J. *Chemical Kinetics*; Harper & Row: New York, 1987.
- (50) Wales, D. J. *J. Chem. Phys.* **2009**, *130*, 204111.
- (51) Stevenson, J. D.; Wales, D. J. *J. Chem. Phys.* **2014**, *141*, 041104.
- (52) Bryngelson, J. D.; Wolynes, P. G. *Proc. Natl. Acad. Sci. USA* **1987**, *84*, 7524–7528.
- (53) Bryngelson, J. D.; Onuchic, J. N.; Socci, N. D.; Wolynes, P. G. *Proteins: Struct., Func. and Gen.* **1995**, *21*, 167–195.

- (54) Leopold, P. E.; Montal, M.; Onuchic, J. N. *Proc. Natl. Acad. Sci. USA* **1992**, *89*, 8721.
- (55) Walsh, T. R.; Wales, D. J. *J. Chem. Phys.* **1998**, *109*, 6691–6700.
- (56) Kumeda, Y.; Wales, D. J. *Chem. Phys. Lett.* **2003**, *374*, 125–131.
- (57) Dijkstra, E. W. *Numerische Math.* **1959**, *1*, 269–271.
- (58) Stone, A. J.; Wales, D. J. *Chem. Phys. Lett.* **1986**, *128*, 501–503.
- (59) Swinburne, T. D.; Wales, D. J. *J. Chem. Theory Comput.* **2020**, *16*, 2661–2679.
- (60) Lecomte, V.; Appert-Rolland, C.; van Wijland, F. *J. Stat. Phys.* **2007**, *127*, 51–106.
- (61) Silva, V. H.; Aquilanti, V.; de Oliveira, H. C.; Mundim, K. C. *Chem. Phys. Lett.* **2013**, *590*, 201–207.
- (62) Naumkin, F. Y. *J. Phys. Chem. A* **2021**, *125*, 5738–5744.
- (63) Adjizian, J.-J.; Vlandas, A.; Rio, J.; Charlier, J.-C.; Ewels, C. P. *Philos. Trans. R. Soc. A* **2016**, *374*, 20150323.
- (64) Parr, R. G.; Szentpály, L. v.; Liu, S. *J. Am. Chem. Soc.* **1999**, *121*, 1922–1924.
- (65) Chattaraj, P. K.; Roy, D. R. *Chem. Rev.* **2007**, *107*, PR46–PR74.
- (66) Clayton, D. D.; Deneault, E. A.-N.; Meyer, B. S. *Astrophys. J.* **2001**, *562*, 480–493.
- (67) Cherchneff, I.; Le Teuff, Y. H.; Williams, P. M.; Tielens, A. G. G. M. *Astron. Astrophys.* **2000**, *357*, 572–580.
- (68) Berné, O.; Tielens, A. G. *Proc. Natl. Acad. Sci. U.S.A.* **2012**, *109*, 401–406.

Graphical TOC Entry

